

Article

Effects of Supercritical CO₂ Treatment Temperature on Functional Groups and Pore Structure of Coals

Zhaolong Ge ^{1,2,*}, Mengru Zeng ^{1,2}, Yugang Cheng ³, Haoming Wang ^{1,2} and Xianfeng Liu ^{1,2}

¹ State Key Laboratory of Coal Mine Disaster Dynamics and Control, Chongqing University, Chongqing 400044, China; zengmengru@cqu.edu.cn (M.Z.); 201820131034@cqu.edu.cn (H.W.); cumtblxf@163.com (X.L.)

² College of Resources and Safety Engineering, Chongqing University, Chongqing 400030, China

³ National and Local Joint Engineering Research Center of Shale Gas Exploration and Development, Chongqing Institute of Geology and Mineral Resources, Chongqing 400042, China; chengyugang@cqu.edu.cn

* Correspondence: gezhaolong@cqu.edu.cn; Tel.: +86-23-651-023-72

Received: 21 November 2019; Accepted: 11 December 2019; Published: 15 December 2019



Abstract: The buried depth of a coal seam determines the temperature at which CO₂ and coal interact. To better understand CO₂ sequestration, the pore structure and organic functional groups of coal treated with different ScCO₂ temperatures were studied. In this study, three different rank coals were treated with ScCO₂ at different temperatures under 8 MPa for 96 h in a geochemical reactor. The changes in pore structure and chemical structure of coal after ScCO₂ treatment were analyzed using mercury intrusion porosimetry, attenuated total reflection Fourier transform infra-red spectroscopy, fractal theory, and curve fitting. The results show that the enhancement effect of ScCO₂ on pore structure of coal becomes less significant as the increase of buried depth. In most of the treated coal samples, the variation proportion of mesopores decreased and the variation proportion of macropores increased. In the relatively higher rank coals, the degree of condensation (DOC) of aromatic rings decreased after treatment with ScCO₂. The DOC values showed a U-shape relationship with temperature, and the aromaticity showed a downward trend with increasing temperature. The chemical structural changes in the relatively lower rank coal sample were complex. These findings will provide an understanding of mechanisms relevant to CO₂ sequestration with enhanced coalbed methane recovery under different geothermal gradients and for different ranks of coal.

Keywords: FTIR spectroscopy; pore structure; supercritical carbon dioxide; geological sequestration; coal rank

1. Introduction

Carbon dioxide capture and sequestration (CCS) is technically and economically feasible, and it will be possible to reduce CO₂ greenhouse gas emissions [1,2]. Geological storage as part of CCS is regarded as the most effective method to store CO₂ [3–5]. A large number of abandoned underground coal mines and deep unmineable coal seams exist worldwide because of resource depletion, low production capacity, and technical limitations. These mines are potential hosts for CO₂ storage and filling material consisting of a mixture of fine-fraction waste [6–8]. Compared to CH₄, CO₂ has higher adsorption capacity and can be stored stably in coal reservoirs [9]. In addition, replacing the CH₄ is conducive to coalbed methane extraction and allows the energy resource in the coal seams to be utilized [10,11]. The potential release of significant quantities of CO₂-enhanced coalbed methane (CO₂-ECBM) has caused widespread concern [5,12,13]. It is estimated that at present, closed mines in China still contain about 42 × 10⁹ tons of coal resources and nearly 500 × 10⁹ cubic meters of unconventional gas [14].

Therefore, it is necessary to make full use of abandoned mine resources and deep unmineable coal seams to achieve CO₂ sequestration [15].

Because most of the shallow coal seams in China have already been mined, the increased demand for coal caused by economic growth has led to the mining of deeper coal seams. When the target coal seam is deeper than 800 m, CO₂ will become the supercritical state (31.06 °C, 7.38 MPa) [16]. The physical properties of CO₂ such as density, viscosity, and diffusivity vary significantly, and there are complex physical and chemical interactions between supercritical carbon dioxide (ScCO₂) and coal [17]. In terms of chemistry, as an organic solvent, ScCO₂ extracts organic and inorganic matter from coal and this significantly affects the contacts between coal particles resulting in the opening of pores, and the macromolecular structure of the coal changes [18–21]. This affects the coal's adsorptive capacity [22,23]. Fourier transform infra-red spectroscopy (FTIR) is a non-destructive method of detecting macromolecular structure of the coal, especially organic functional groups [24]. Zhang et al. [25,26] found that the functional group intensities of coal weakened significantly after ScCO₂ treatment, indicating that ScCO₂ extraction occurred. These studies qualitatively judge the weakening of the functional group intensities. Changes in the coal's macromolecular structure were not considered, which can be deeply semi-quantitative analyzed through curve-fitting. Physically, the coal's structure will be transformed and rearranged due to the changes in its pore structure, resulting in its mechanical properties altered [27]. In addition, the coal matrix will swell because of the CO₂ adsorption, which will reduce the number and width of cracks and seepage channels in some coal reservoirs [28,29]. The effect of the above on the fracture width (W) is expressed as follows [25]:

$$W = -W_1 + W_2 - W_3 + W_4, \quad (1)$$

where W_1 is external stress, W_2 is CO₂ injection pressure, W_3 is adsorption expansion effect, and W_4 is ScCO₂ extraction effect. The coal's pore structure will change significantly, and this affects the CO₂ storage capacity in the seam.

The coal's burial depth determines the final temperature of the injected CO₂. Some researchers have shown that both coal reservoir permeability and gas adsorption/desorption are significantly affected by temperature [30–34]. Several studies reveals that higher reservoir temperatures result in bond breaks between gas molecules and coal's surface [35–38]. Finally, after gas is released from the coal, the gas adsorption capacity in the coal is reduced. Coal matrix swells due to CO₂ adsorption, and gas diffusion and seepage channels are reduced [29]. Therefore, temperature influences the pore structure and the macromolecular structure of coal significantly, which needs to be discussed in detail.

Previous research has focused on changes in the pore structure of coal with different coal rank after ScCO₂ exposure. ScCO₂ increased the macropore volume of coal accompanied by a reduction in minerals, extraction of hydrocarbons, and weakening of mechanical properties. These experiments were conducted at a single temperature. The properties of ScCO₂ such as density, viscosity, and diffusivity will change with the growing depth of the coal seams at different temperatures, and this may cause different results from previous studies that have not considered the temperature change. To date, the effects of temperature on coals affected by ScCO₂ remain largely unreported in the literature. More efforts are needed to understand the interactions between ScCO₂ and coal [39].

In this study, mercury intrusion porosimetry (MIP), and attenuated total reflection Fourier transform infra-red spectroscopy (ATR-FTIR) tests were used to determine the changes in the chemical functional groups and physical pore structure of three bituminous coal samples under a range of ScCO₂ temperatures. The structural parameters of coals were further discussed through curve fitting and fractal theory, which are not commonly used in the previous studies. The aim of the study is to better understand how ScCO₂ at different temperatures affects the interaction between CO₂ and different rank coals. These results can guide further assessment of geological CO₂ sequestration with enhanced coalbed methane recovery.

2. Materials and Methods

2.1. Sample Collection

For this study, three coal samples from different mines were obtained, one from the Nanchuan coal mine in Chongqing (NC) and one each from the Jincheng coal mine (JC) and the Datong coal mine (DT) in Shanxi province. The general locations of the coal mines are shown in Figure 1. The vitrinite reflectance (R_o) analyses were performed on an Axio Scope A1 (Carl Zeiss Instruments, Oberkochen, Germany) following the standard ISO 7404-5:2009. The proximate analysis was carried out on a proximate analyzer (Changsha Kaiyuan Instruments, Changsha, China) according to the International Standard ISO 17246:2010. The analyses are shown in Table 1.

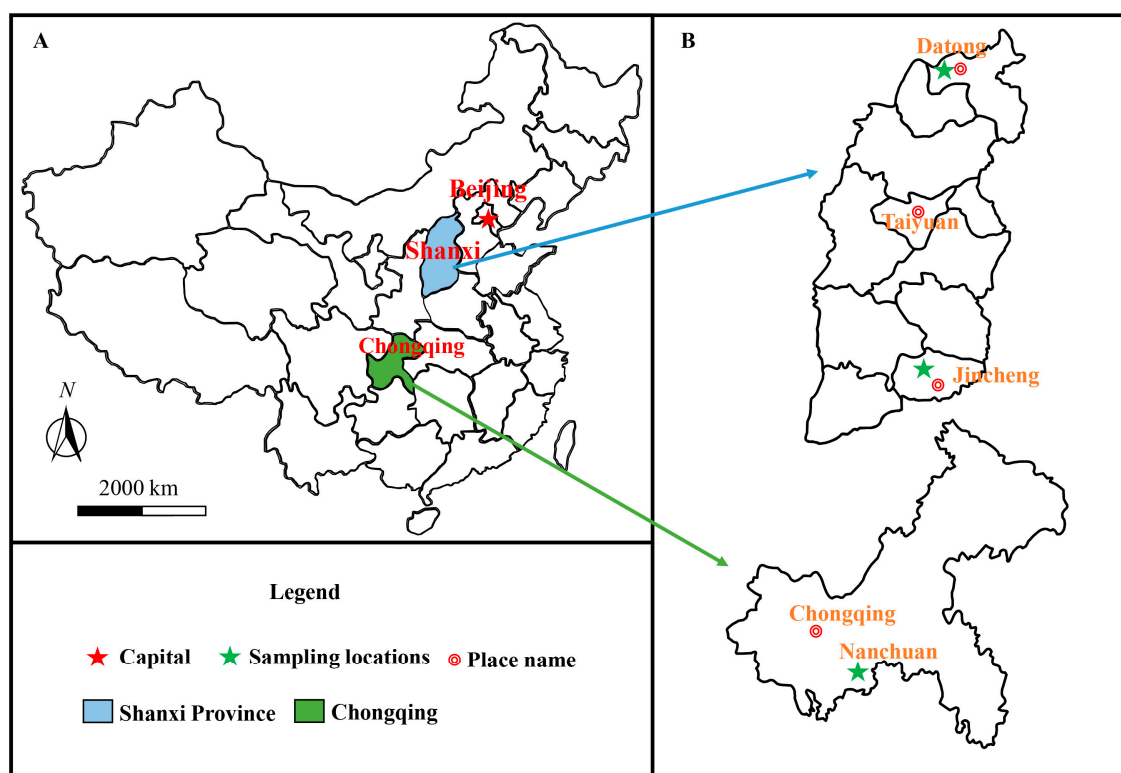


Figure 1. Map of China showing the locations of the coal mines from which the samples were collected. (A) Map of China; (B) Map of Shanxi province and Chongqing.

Table 1. Properties of the coal samples.

Sample	Sampling Location	Proximate Analysis (wt %)				R_o (%)	Coal Rank
		M_{ad}	A_{ad}	V_{daf}	FC_{ad}		
NC	Nanchuan, Chongqing	0.89	8.27	30.14	60.70	1.105	Bituminous Coal B
JC	Jincheng, Shanxi	0.98	5.53	31.26	62.23	1.051	Bituminous Coal B
DT	Datong, Shanxi	2.41	9.46	36.22	51.91	0.683	Bituminous Coal C

Note: M_{ad} , moisture; A_{ad} , ash; V_{daf} , volatile matter; FC_{ad} , fixed carbon. daf = dry ash free. Nanchuan coal mine in Chongqing (NC), Jincheng coal mine (JC), Datong coal mine (DT).

The coal samples were crushed, fully mixed, and sieved to a -3 mm grain size. For the experiments, the samples were divided into two even parts (ScCO₂ treated sample, untreated sample) for comparison.

2.2. ScCO₂ Treatment

The geothermal gradient of deep coal seams (>800 m) is generally 1–3 °C/hm. At present, the actual mining depth of deep coal seams in China is up to 1500m, where the reservoir temperature is about 70 °C [34]. With the growing demand for deep mining (>1900 m), CO₂ may be stored in deeper coal seams at temperatures of up to 80 °C in the future. Thus, the test temperature in this experiment was taken as 40–80 °C. In order to better compare the effects of temperature on three coal samples, the experimental pressure was only set to 8 MPa according to the coalbed methane (CBM) logging data [40]. The experimental parameters are listed in Table 2.

Table 2. Experimental conditions.

Sample	Treated Time (h)	Temperature (°C)	Pressure (MPa)
	-	-	-
NC/JC/DT	96	40	8
	96	50	8
	96	60	8
	96	70	8
	96	80	8

The ScCO₂ treatment experiments were conducted using a geochemical reactor that can simulate CO₂ injection into a coal reservoir. The experimental setup is illustrated in Figure 2. The system consists of five main parts: a constant temperature water bath, a vacuum pump, a control panel and pipeline system, a pressure gauge, and a compression and gas injection system.

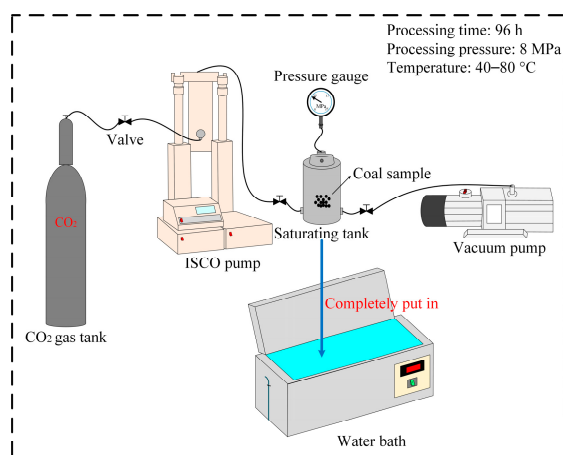


Figure 2. Schematic diagram showing the equipment that constitutes the geochemical reactor.

During an experiment, the saturating tank was first put into the constant temperature water bath which was heated to the target test temperature and the coal sample was degassed by the vacuum pump for 8 h. Then, the saturating tank was filled with CO₂ via the ISCO pump (Teledyne ISCO, Lincoln, NE, USA) (10 mL/min). The final pressure of the sample tank after filling was 8 MPa. Meng and Qiu [27] concluded that changes of coal's properties can be fully observed at 72 h. Liu et al. [19] proposed that the reaction between ScCO₂ and coal in the first 60 h is sufficient. In this study, the reaction time was 96 h to make sure of a sufficient reaction process. The experimental condition was maintained at the target value listed in Table 2. After 96 h, the tank was slowly depressurized and the coal samples were taken for subsequent testing.

2.3. MIP Tests and Fractal Dimension Calculation(D)

The pore structure of the coal samples was performed using a Quantachrome PoreMaster-33 mercury porosimeter (Quantachrome Instruments, Boynton Beach, FL, USA). The pressure range of the equipment is 0.14–231 MPa. MIP can determine the pore size distribution from 6.4 nm to 950 μm , which is widely used for analyzing the pore structure of porous medium such as shale and coal. The particle size of the coal sample used for MIP testing was 3–5 mm.

Fractal dimension can characterize the surface roughness and internal complexity of porous media. Based on the fractal theory, the coal's pore structure is further analyzed using the MIP data. The D value can be calculated from the Equation (2) [41]:

$$\ln V = (3 - D) \ln(P - P_t) + \ln A, \quad (2)$$

where V represents the cumulative intrusion volume of mercury (cm^3/g); D denotes the fractal dimension; P denotes the mercury pressure (MPa); P_t denotes the threshold pressure of mercury (MPa); and A represents a constant.

2.4. Curve-Fitting Analysis of ATR-FTIR Spectra

The ATR-FTIR tests were performed using a Nicolet iS50 type Fourier infrared spectrometer (Thermo Fisher Scientific, Waltham, MA, USA). Thirty two scans per spectrum were collected at a resolution of 4 cm^{-1} over a scanned range of $650\text{--}4000 \text{ cm}^{-1}$. The air spectrum was used as a background for each sample. The particle size of the coal sample used for ATR-FTIR testing was $74 \mu\text{m}$.

Each spectrum is made up of multiple superimposed functional peaks. It is difficult to distinguish the position and the proportion of the absorption peaks in different regions. In order to better analyze the functional groups, the spectra were divided into three regions that have been used by other researchers for semi-quantitative analysis. These regions are aliphatic structures ($3000\text{--}2800 \text{ cm}^{-1}$), oxygen-containing structures ($1800\text{--}1000 \text{ cm}^{-1}$), and out-of-plane aromatic C-H structures ($900\text{--}700 \text{ cm}^{-1}$) [24]. The peaks were assigned following the work by Painter et al. [42] The peak analysis was performed using Peakfit V4.12 software (SeaSolve Software, Inc., San Jose, CA, USA). Based on the shape of the bands, the spectra were fitted by a combination of Gaussian and Lorentz functions [24,43].

Semi-quantitative parameters, “ L ”, “ I ”, and “DOC” (identified in Table 3 and described in the following sections) were obtained via curve-fitting of the FTIR spectra in order to investigate the coal's chemical properties.

Table 3. Infrared indexes from ATR-FTIR spectra used to investigate the structure of hydrocarbons in the coal [44].

IR Index	Band Region (cm^{-1})	Index Meaning
L	A_{2925}/A_{2950}	Aliphatic chain length/Degree of branch chain
I	$A_{700-900}/A_{2800-3000}$	Aromaticity
DOC	$A_{700-900}/A_{1600}$	Degree of condensation (DOC) of aromatic rings

3. Results and Discussion

3.1. MIP Analyses

3.1.1. Variations in Pore Volume

The pore volumes of the coal specimens have been divided according to the aperture classification method proposed by B.B Hodot [45], i.e., micropores (<10 nm), minipores (10–100 nm), mesopores (100–1000 nm), and macropores (>1000 nm). This method is widely used in China [25,46,47]. In this study, pores are divided into four parts (total pores, macro-, meso-, and micro+minipores). The volumes

of different types of pores were calculated according to the cumulative amount of mercury injected in each aperture. The variation proportion in each pore size class after ScCO₂ treatment was calculated by Equation (3).

$$\text{Variation proportion} = (V_{\text{treatment}} - V_{\text{raw}}) / V_{\text{raw}} \times 100\%, \quad (3)$$

where $V_{\text{treatment}}$ is pore volumes of ScCO₂ treated coal sample; V_{raw} is pore volumes of untreated coal sample.

Figure 3a–c shows all the variation proportion of total pores in the treated samples are positive. This indicates that ScCO₂ increases the pore size of coal. Given that water existed in the raw coal, CO₂ dissolved in water formed carbonic acid during ScCO₂ exposure [48,49]. Jiang et al. [50] found that crystal water was released from clay minerals after ScCO₂ treatment. Previous studies have shown that some carbonate minerals are dissolved and some hydrocarbons are extracted and washed away by the gas or water after ScCO₂ treatment [23,26]. The chemical reactions are listed in Equations (4) and (5). Apparently, many pores originally separated by minerals and hydrocarbons become continuous pores. Theoretically, CO₂ is adsorbed in the coal seam while CH₄ is replaced simultaneously. These continuous pores are conducive to CH₄ desorption and flow. Therefore, CO₂ could enhance coalbed methane recovery and can be stored in the coal seam [26].

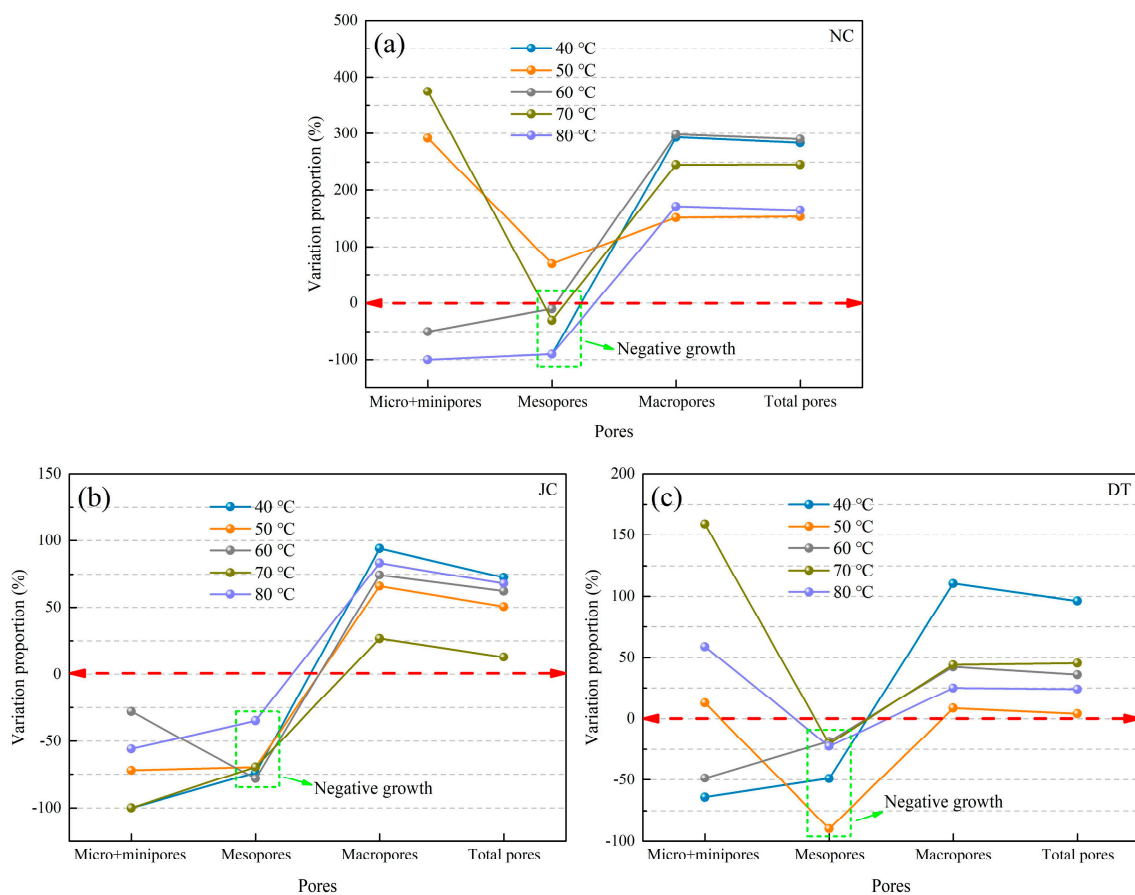
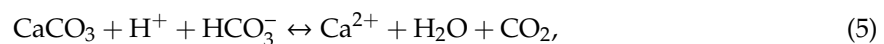


Figure 3. Variation proportion in each pore size class after ScCO₂ treatment. (a) NC; (b) JC; (c) DT. Nanchuan coal mine in Chongqing (NC), Jincheng coal mine (JC), Datong coal mine (DT).

The total pore volume in the samples treated with ScCO₂ at 40 °C is almost the largest pore volume of all the temperatures tested. After ScCO₂ treatment, the total pore volume of the NC, JC, and DT samples increased by 284%, 73%, and 96%, respectively. These results indicate that treatment at 40 °C has a great influence on the expansion of the seepage channels and the pore structure. The variation proportion of total pores decreases with as temperature increases. In conclusion, as the increase of buried depth, the enhancement effect became less significant. This is because temperature influences the supercritical fluid density. Under the same pressure, the density of ScCO₂ decreases as temperature increases, and the solubility of ScCO₂ decreases [50,51].

As seen in Figure 3, the value of variation proportion less than zero is defined as a “negative growth” region. The variation proportion of mesopores change is negative in almost all cases and the variation proportion of macropores change is always positive. It may be that the transformation of micro- and minipores to the mesopores is less complete than the transformation of micro-, mini-, and mesopores to macropores. Regardless of temperature effects, the increase in macropores is consistent with previous research [19,27,52]. The difference in the results of other pores is due to the complexity of coal’s pore structure.

3.1.2. Variations in Fractal Dimension (D)

The mercury injection curves are divided into three stages (Figure 4a) using the fractal divisions of mercury injection curves proposed by Liu et al. [19]. The stages A and B represent the microfissures (48.86–187.7 μm) and microcracks (8.428–48.86 μm) of the coal samples filled with mercury in the low-pressure injection process. Stage C shows the mercury enters the pores (9.61 nm–14.76 μm) in the high-pressure injection process. As described in Equations (2) and (3), the *D* value is obtained [41]. Figure 4b–d gives the ln(*V*) vs. ln(*P*–*P*_t) for fractal dimension analysis. The *D* values (*D*₁, *D*₂, *D*₃) represent the fractal dimension of these three stages (A, B, C) of each coal sample, respectively. A larger *D* value indicates a rougher and more irregular surfaces [53].

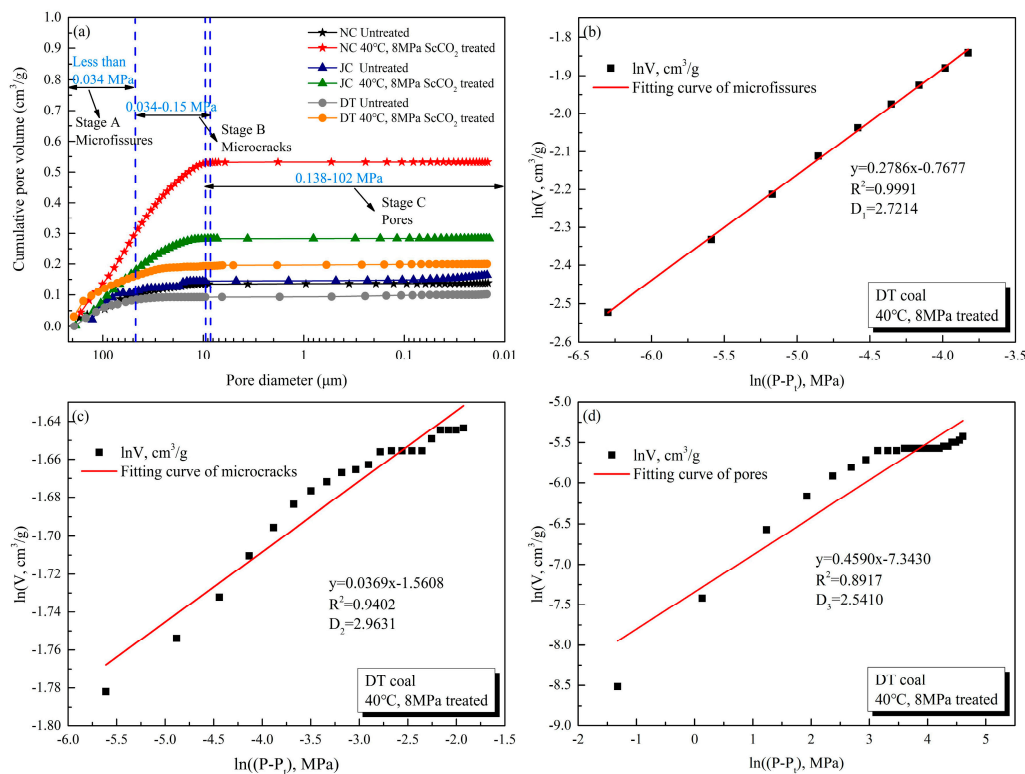


Figure 4. (a) Mercury injection curve from mercury intrusion porosimetry (MIP) tests on the coal samples; (b–d) ln(*V*) vs. ln(*P*–*P*_t) for fractal dimensions *D*₁ (b); *D*₂ (c); and *D*₃ (d).

As shown in Figure 5, the results show that most D_1 values are lower at higher ScCO_2 treatment temperatures, indicating that the complexity and surface roughness of microfissures gradually decrease with increasing temperature. D_2 values are all between 2.8 and 3.0, which show that the microcracks are more complicated. After ScCO_2 treatment, D_2 values decrease, indicating that ScCO_2 treatment reduces the complexity of microcracks. D_3 values fluctuate greatly because stage C reflects the compression process at high pressure [54,55]. The blue dashed lines in Figure 5 marks the smaller D values, which represents a less complex pore structure. According to previous research, the coal surface becomes smoother after extraction effect of ScCO_2 [12,23,56]. The ScCO_2 reduced the DT coal's pore structure complexity (the fractal dimension) when the coal was treated at higher temperatures of 70 °C and 80 °C, but the fractal dimension of the NC and JC coals appeared to exhibit an opposite trend at 50 °C and 70 °C, and 60 °C and 80 °C, respectively. It can be inferred that the higher the coal rank, the lower the favorable temperature range for ScCO_2 to reduce pore complexity.

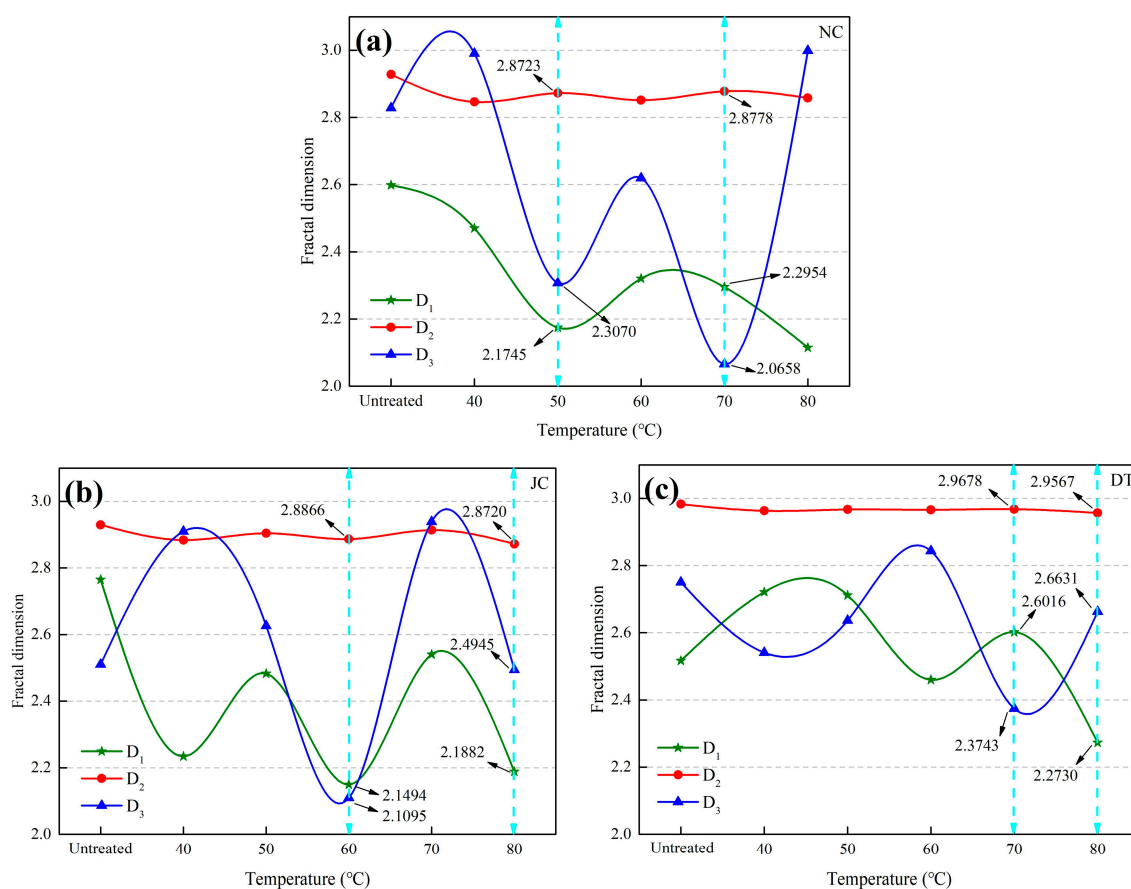


Figure 5. Variation trends of coal sample fractal dimensions (D_1 , D_2 , D_3) of three coal samples at different temperatures. (a) NC; (b) JC; (c) DT.

3.2. ATR-FTIR Analyses

The ATR-FTIR spectra from the treated and untreated coal samples at different temperatures are shown in Figure 6. The sample's infrared spectra are similar, but the intensities of the absorption peaks are different. This indicates that the amounts and composition of those structures in the three coal samples differ. The peaks for the $-\text{OH}$ groups ($3600\text{--}3100\text{ cm}^{-1}$) and oxygen-containing structures ($1800\text{--}1000\text{ cm}^{-1}$) in the DT coal are higher than those peaks in the NC and JC coals. In addition, the aromatic C-H stretching vibration peak ($3100\text{--}3000\text{ cm}^{-1}$) from the DT coal is lower than that peak from the other two coals. The aliphatic hydrocarbon content (represented by the $3000\text{--}2800\text{ cm}^{-1}$ peak) increases with the decreasing coal rank. The 1306 cm^{-1} absorption peak is not present for the DT coal sample. The peak's disappearance is related to the chemical and physical structural changes caused

by a coalification jump [57,58]. The absorbance of the NC and JC samples in the aromatic structure reflectance range ($900\text{--}700\text{ cm}^{-1}$) is greater than that of the DT sample. The organic functional group intensities weakened after ScCO_2 treatment, indicating that some chemical changes must have taken place, such as organic molecule extraction. The oxygen-containing functional groups were reduced after ScCO_2 exposure. The reduction of organic substances results in the transformation of open micro- and mesopores near the macropores into macropores. The peak fitting results for the NC coal sample after ScCO_2 treatment at 40°C and 8 MPa are shown in Figure 7. The errors of parameters extracted from ATR-FTIR spectra are within $\pm 5\%$.

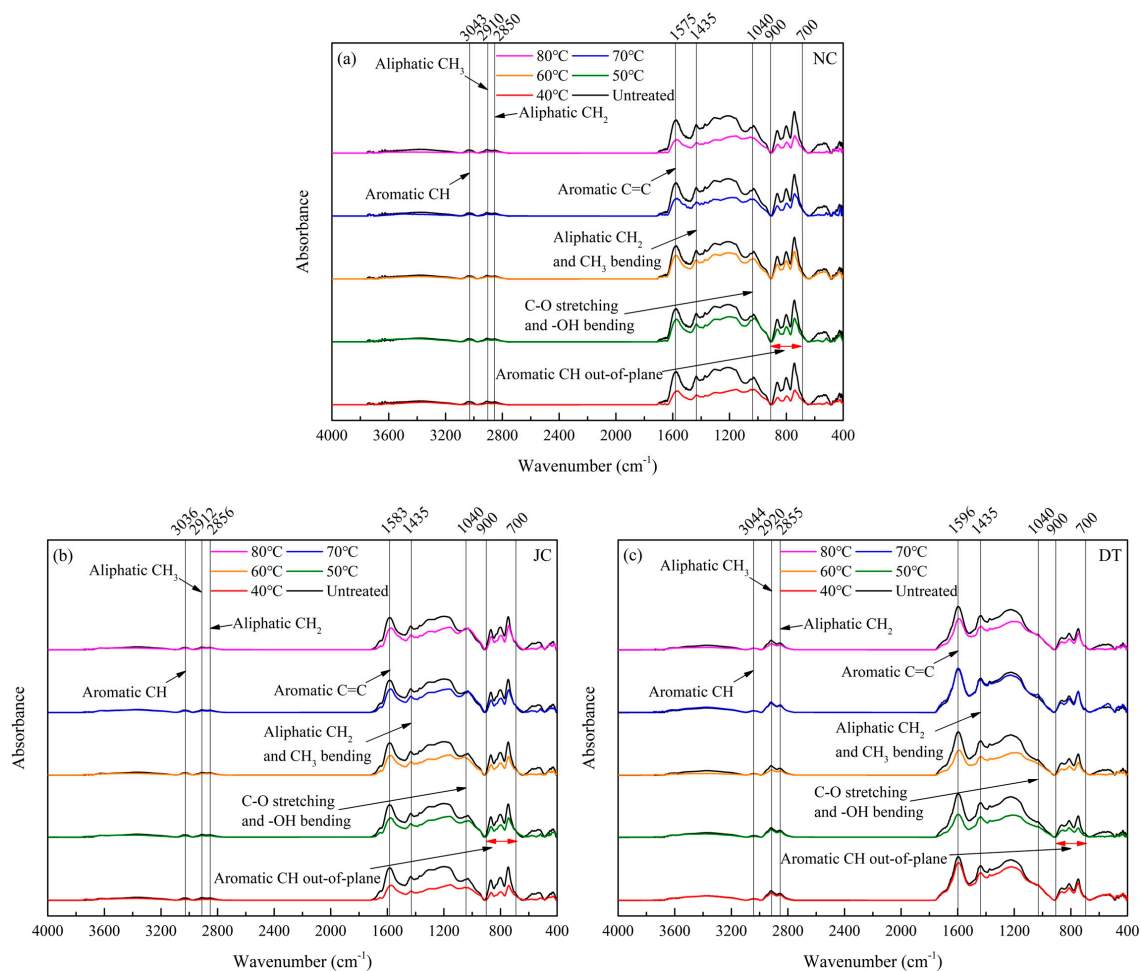


Figure 6. ATR-FTIR spectra of coal samples treated with ScCO_2 . (a) NC; (b) JC; (c) DT.

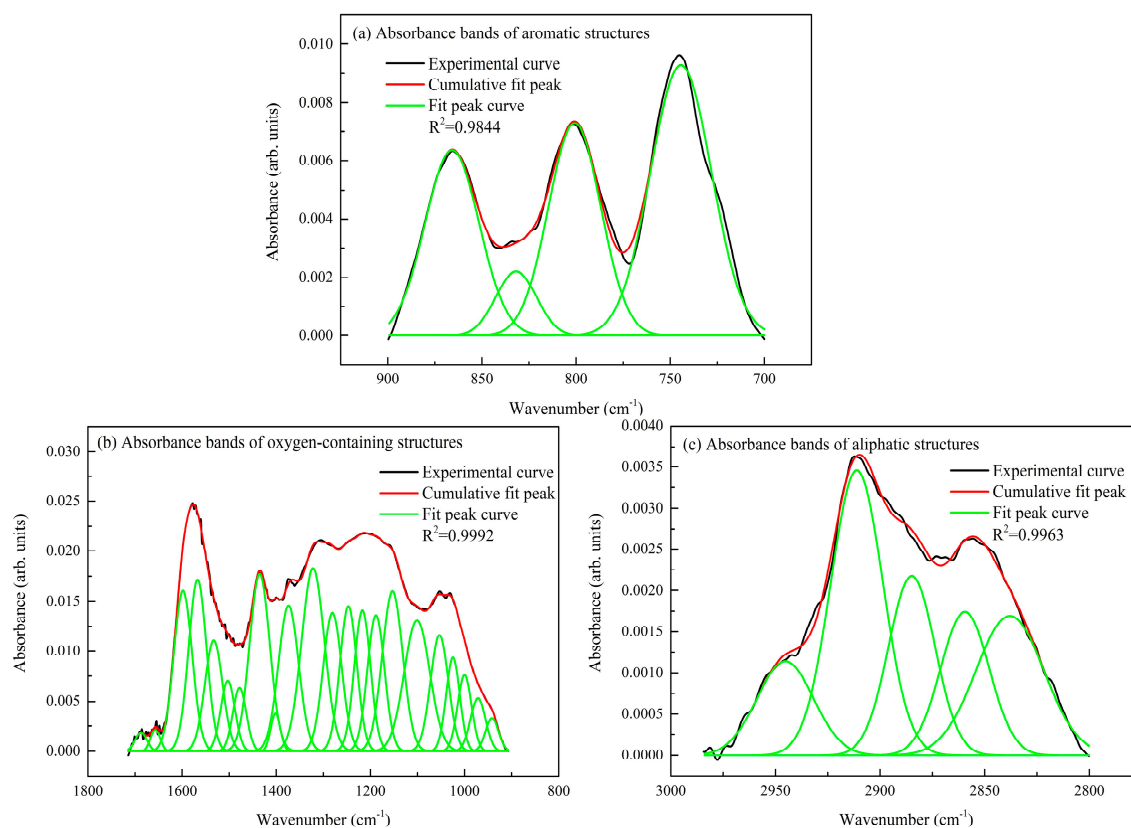
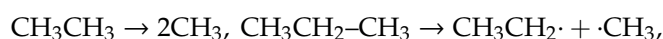
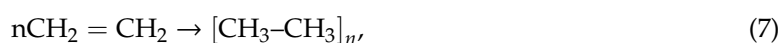
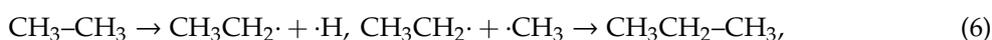


Figure 7. Curves fit to the ATR-FTIR spectrum from NC coal after ScCO₂ treated at 40 °C and 8 MPa.

3.2.1. Variations in Aromaticity

The “*I*” IR index represents the intensity of aromatic structures relative to aliphatic structures [24]. Figure 8 shows the *I* (aromaticity), *L* (aliphatic chain length), and degree of condensation (DOC) of aromatic rings indexes and shows that the NC and JC coals contain more aromatic hydrocarbons than aliphatic hydrocarbons. However, the DT coal contains more aliphatic hydrocarbons, and this means that the aliphatic hydrocarbons content increases gradually as the coal rank decreases. The *I*-values for the NC and JC samples show a general downward trend with increasing temperature but the changes in DT coal sample *I*-values is more complicated. Previous research has shown that low-rank coal is excited more by ScCO₂ treatment than high-rank coal, and that coal rank affects the aromatic and aliphatic hydrocarbon content of the coal [18,23]. Aliphatic structures were easier to be mobilized than aromatic structures. CO₂ is a non-polar molecule. According to the similar phase dissolution-relationship, CO₂ is easier to chemically react with non-polar bonds or weakly polar bonds. Small aliphatic molecules are bonded with some weak noncovalent bonds, such as hydrogen bonds or other even weaker interactions. More aliphatic hydrocarbons in DT coal is responsible for more complex chemical reactions in lower rank coal, such as dissociation reactions, addition reactions, polyaddition reactions, or substitution reactions [59]. In addition, lower rank coal may be more sensitive to temperature and it is easier to react with ScCO₂ than higher rank coal. This is the reason why the distribution of DT coal *I*-values is relatively irregular. The chemical reactions that may occur in ScCO₂ and coal are listed in Equations (6)–(8).



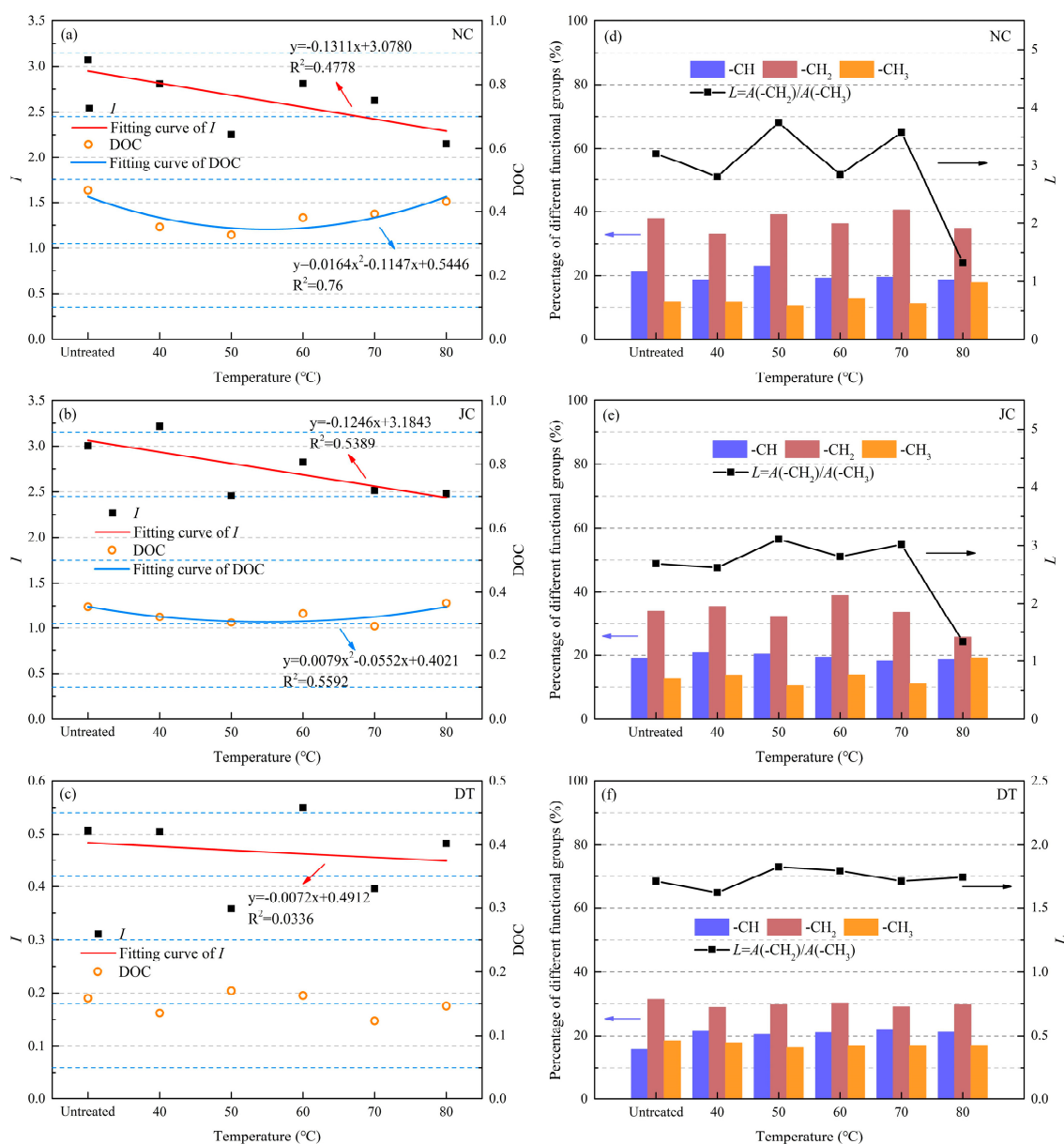
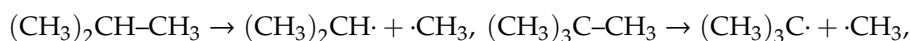
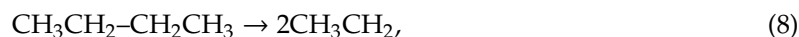


Figure 8. Graphs of IR indexes of the coal samples. (a–c), I and DOC; (d–f), percentage of different aliphatic hydrocarbon groups and change in L. See text for a description of the IR indexes.

The hydrogen free radical ($\cdot\text{H}$) resulted from cross-link breakage can be substituted by CH_x , and the aromatic- CH_x (Ar-CH_x) and aliphatic- CH_x forms (Equation (6)). The formation of C–C cross-links is a polyaddition reaction (Equation (7)). In addition, the free radical ($\cdot\text{C}$) can be formed by the chemical bond of CH_x under acid environment and heating condition [60]. This is the bond dissociation reaction of CH_x (Equation (8)).

3.2.2. Variations in the DOC of Aromatic Rings

Figure 8 clearly shows that the DOC of aromatic rings increases as coal rank increases. The DOC-values for the NC and JC samples are much higher than the DT DOC-values. Liu et al. [59]

also found that the DOC-values decrease after ScCO₂ treatment, but the reason was not given in the literature. The U-shape relationship between temperature and DOC is also clear in Figure 8. According to the *I*-values, the relative contents of aliphatic and aromatic hydrocarbons changed after ScCO₂ treatment. Thus, changes in the coal's macromolecular structures cause the DOC-values to decrease. The DOC-values increase in the 60–80 °C range due to the molecular activation energy decreases and the intermolecular collision intensifies at higher temperatures. At 80 °C, the aliphatic side chains in the NC and JC coals are shorter, resulting in relatively compact structures with small spaces between the aromatic clusters [61]. At 80 °C, the DOC-values are higher than they are at lower temperatures.

The DOC of the aromatic rings increases as coal rank increases, resulting in a denser coal skeleton. Changes in the coal skeleton cause the coal to be compacted [62,63]. Therefore, an increase in the DOC-values indirectly results in the compaction of the coal bulk. After ScCO₂ exposure, the decrease in the DOC-values indicates a relatively loose coal structure due to the extraction of the polycyclic aromatic hydrocarbons, the aliphatic hydrocarbons, and the aromatic hydrocarbons. Fu et al. [64] reported that an increase in the DOC of aromatic rings favors CH₄ adsorption. Therefore, the decrease in the DOC-values after ScCO₂ treatment favors CH₄ desorption.

3.2.3. Variations in Aliphatic Chain Length and Aliphatic Hydrocarbon Content

The “*L*” value is the ratio between the CH₂ and CH₃. This represents the length or degree of the aliphatic side chains. Figure 8d–f shows the changes in the *L*-value and the percentage of aliphatic hydrocarbon groups in the treated and raw coal samples. The *L*-value of untreated coal samples increases with coal rank. The macromolecular structure of these samples is dominated by –CH₂. This indicates that straight chains and alicyclic structures with few branches exist in the aliphatic hydrocarbons of the coal samples [60].

The trend of the NC and JC aliphatic chain lengths changes is basically the same. This is because they belong to the same coal rank. The fluctuation of the *L*-values indicates that at different temperatures, the aliphatic hydrocarbon side chains not only break and fall off, but the hydrocarbons also undergo different degrees of addition and polyaddition reactions. An example of cross-linked cluster generation can be found in the work by Carstro-Marcano et al. [65].

At 80 °C, the NC and JC chain lengths decrease by 58.89% and 50.38% respectively, which may be because the higher temperature encourages the side chains to fall off the –CH₂ groups. The *L*-values of DT coal treated with ScCO₂ are higher than the *L*-value of the untreated DT coal sample (except for the DT coal treated at 40 °C). The percentages of –CH₂ and –CH₃ in the DT coal generally decrease as the treatment temperature increases, but the decrease in –CH₂ is less than –CH₃. There are no obvious changes in the functional subgroups (–CH₃, –CH₂, and –CH) obtained from the aliphatic structures represented by the 3000–2800 cm^{–1} band. The changes that take place in the different coal samples at different ScCO₂ treatment temperatures are complicated. This complexity arises from the complex chemical properties of ScCO₂ fluids and coals.

In addition, under the pressure exerted by the surrounding rock, the functional groups and side chains in the coal may break and generate free radicals. These free radicals adhere to the cracks and internal surfaces in the coal and can combine with O₂ to form CO [66]. Mazumder et al. [67] have shown that there is a high probability that coal and CO₂ will react to form CO when CO₂ is stored in coal seams. The newly generated CO, the aliphatic and aromatic hydrocarbons, and the polycyclic aromatic hydrocarbons in the coal matrix extracted by the ScCO₂ are biologically toxic. These substances dissolved in gas and water will enter the coal seams, the rock formations, and the groundwater surrounding the coal seam and will become environmental hazards [23,68].

The functional groups and the coal's internal structure changed after ScCO₂ treatment indicating that chemical reactions occurred. Furthermore, the chemical changes and degrees of structural change in the three samples were not the same because the samples were not of the same rank. The changes in the macromolecular structure that took place in the relatively higher rank coals at different ScCO₂ treatment temperatures were relatively simple but the changes in the relatively lower rank coal were

more complex. Research has shown that ScCO₂ extracted more organic material from low rank coal than it extracted from high rank coal. [10,23,68] CO₂ Storage in low-rank coal seams will have more environmental issues. Additional research should be done on low-rank coal–ScCO₂ reactions.

4. Conclusions

In this study, MIP test, fractal theory, ATR-FTIR test, and curve fitting were conducted on three coal samples to understand the effects of supercritical carbon dioxide (ScCO₂) treatment on the pore structure and functional groups in the coal at different temperatures. The conclusions were drawn as follows:

- (1) The cumulative pore volume of the three coal samples treated with ScCO₂ increases significantly. In most of the treated coal samples, the variation proportion of mesopores decreases and the variation proportion of macropores increases. Compared to the untreated coal samples, the total pore volumes in samples treated with ScCO₂ at 40 °C (the NC, JC, and DT samples) increased by 284%, 73% and 96%, respectively. In general, compared to the treatment at any other temperature, the pore structure of coal develops better when the ScCO₂ is 40 °C. The variation proportion of total pores decreases with increasing temperature. In conclusion, as the buried depth increased, the enhancement effect of ScCO₂ became less significant.
- (2) The ScCO₂ reduced the DT coal's pore structure complexity (the fractal dimension) when the coal was treated at higher temperatures (70 °C and 80 °C), but the fractal dimension of the NC and JC coals appeared to exhibit an opposite trend in the 50 °C and 70 °C, and 60 °C and 80 °C. The higher the coal rank, the lower the favorable temperature range for ScCO₂ to reduce pore complexity.
- (3) When measured by FTIR, the hydrocarbon functional group IR peaks from the three ScCO₂-treated coal samples are lower than the peaks from the untreated samples because the ScCO₂ extracted some hydrocarbons. The structural parameters of the coal samples were classified using three IR indexes: *L* (aliphatic chain length), *I* (aromaticity), and degree of condensation (DOC) of aromatic rings. These indexes were obtained by curve fitting. After treatment with ScCO₂, the *I*-values for the NC and JC coals decreased when the temperature is increased. The DOC-values of those two samples are lower and the DOC-values follow a U-shape curve with temperature. The decrease in the DOC-values indicates a favorable desorption of CH₄. However, no regular patterns in the IR index data for the DT coal sample were apparent, implying that the changes in the relatively lower rank coal during ScCO₂ treatment are more complex. The changes in aliphatic chain lengths in the NC and JC coal samples are consistent. Almost all of the *L*-values of the ScCO₂-treated coal sample (DT) are higher than the *L*-values of untreated samples.

Both CO₂ sequestration and CO₂-ECBM are affected by many factors. In this study, only the effects of ScCO₂ on coal at different temperatures were investigated. Further effort is needed to investigate the effects of ScCO₂ on coal under different water contents in our next work.

Author Contributions: Z.G. and M.Z. conceived and designed the experiments; M.Z., H.W. and X.L. performed the experiments; M.Z. and Y.C. analyzed the data; Z.G. and W.W. contributed materials and analysis tools; Z.G. and M.Z. wrote the paper.

Funding: This research was funded by the National Natural Science Foundation of China (No. 51774055, 51904049, 51625401); and the Natural Science Foundation of Chongqing (General Program, No. cstc2019jcyj-msxmX0702).

Conflicts of Interest: The authors declare no conflict of interest.

References

1. Pacala, S.; Socolow, R. Stabilization wedges: Solving the climate problem for the next 50 years with current technologies. *Science* **2004**, *305*, 968–972. [[CrossRef](#)] [[PubMed](#)]
2. Chen, W.Y.; Xu, R.N. Clean coal technology development in China. *Energ Policy* **2010**, *38*, 2123–2130. [[CrossRef](#)]

3. Prabu, V.; Mallick, N. Coalbed methane with CO₂ sequestration: An emerging clean coal technology in India. *Renew. Sustain. Energy Rev.* **2015**, *50*, 229–244. [[CrossRef](#)]
4. Singh, H.; Cai, J. A mechanistic model for multi-scale sorption dynamics in shale. *Fuel* **2018**, *234*, 996–1014. [[CrossRef](#)]
5. Su, E.; Liang, Y.; Zou, Q.; Niu, F.; Li, L. Analysis of Effects of CO₂ Injection on Coalbed Permeability: Implications for Coal Seam CO₂ Sequestration. *Energy Fuels* **2019**, *33*, 6606–6615. [[CrossRef](#)]
6. Wang, K.R.; Xu, T.F.; Wang, F.G.; Tian, H.L. Experimental study of CO₂-brine-rock interaction during CO₂ sequestration in deep coal seams. *Int. J. Coal Geol.* **2016**, *154*, 265–274. [[CrossRef](#)]
7. Skrzypkowski, K. Compressibility of materials and backfilling mixtures with addition of solid wastes from flue-gas treatment and fly ashes. *E3S Web Conf.* **2018**, *71*, 00007. [[CrossRef](#)]
8. Skrzypkowski, K.; Korzeniowski, W.; Poborska-Mlynarska, K. Binding capability of ashes and dusts from municipal solid waste incineration with salt brine and geotechnical parameters of the cemented samples. *Arch. Min. Sci.* **2018**, *63*, 903–918. [[CrossRef](#)]
9. Benson, S.M.; Surlles, T. Carbon dioxide capture and storage: An overview with emphasis on capture and storage in deep geological formations. *Proc. IEEE* **2006**, *94*, 1795–1805. [[CrossRef](#)]
10. White, C.M.; Smith, D.H.; Jones, K.L.; Goodman, A.L.; Jikich, S.A.; LaCount, R.B.; DuBose, S.B.; Ozdemir, E.; Morsi, B.I.; Schroeder, K.T. Sequestration of carbon dioxide in coal with enhanced coalbed methane recovery—A review. *Energy Fuels* **2005**, *19*, 659–724. [[CrossRef](#)]
11. Liu, X.; Nie, B.; Wang, W.; Wang, Z.; Zhang, L. The use of AFM in quantitative analysis of pore characteristics in coal and coal-bearing shale. *Mar. Petrol. Geol.* **2019**, *105*, 331–337. [[CrossRef](#)]
12. Bae, J.S.; Bhatia, S.K.; Rudolph, V.; Massarotto, P. Pore Accessibility of Methane and Carbon Dioxide in Coals. *Energy Fuels* **2009**, *23*, 3319–3327. [[CrossRef](#)]
13. Cai, C.; Kang, Y.; Wang, X.; Hu, Y.; Chen, H.; Yuan, X.; Cai, Y. Mechanism of supercritical carbon dioxide (SC-CO₂) hydro-jet fracturing. *J. CO₂ Util.* **2018**, *26*, 575–587. [[CrossRef](#)]
14. Liang, Y. Promote the precise development and utilization of closed/abandoned mine resources in China. *Coal Econ. Res.* **2019**, *39*, 1. [[CrossRef](#)]
15. Ehlig-Economides, C.; Economides, M.J. Sequestering carbon dioxide in a closed underground volume. *J. Pet. Sci. Eng.* **2010**, *70*, 123–130. [[CrossRef](#)]
16. Massarotto, P.; Golding, S.D.; Bae, J.S.; Iyer, R.; Rudolph, V. Changes in reservoir properties from injection of supercritical CO₂ into coal seams—A laboratory study. *Int. J. Coal Geol.* **2010**, *82*, 269–279. [[CrossRef](#)]
17. Okolo, G.N.; Neomagus, H.W.J.P.; Everson, R.C.; Roberts, M.J.; Bunt, J.R.; Sakurovs, R.; Mathews, J.P. Chemical-structural properties of South African bituminous coals: Insights from wide angle XRD-carbon fraction analysis, ATR-FTIR, solid state C-13 NMR, and HRTEM techniques. *Fuel* **2015**, *158*, 779–792. [[CrossRef](#)]
18. Kolak, J.J.; Burruss, R.C. Geochemical investigation of the potential for mobilizing non-methane hydrocarbons during carbon dioxide storage in deep coal beds. *Energy Fuels* **2006**, *20*, 566–574. [[CrossRef](#)]
19. Liu, C.J.; Wang, G.X.; Sang, S.X.; Gilani, W.; Rudolph, V. Fractal analysis in pore structure of coal under conditions of CO₂ sequestration process. *Fuel* **2015**, *139*, 125–132. [[CrossRef](#)]
20. Liu, C.J.; Wang, G.X.; Sang, S.X.; Rudolph, V. Changes in pore structure of anthracite coal associated with CO₂ sequestration process. *Fuel* **2010**, *89*, 2665–2672. [[CrossRef](#)]
21. Liu, S.; Ma, J.; Sang, S.; Wang, T.; Du, Y.; Fang, H. The effects of supercritical CO₂ on mesopore and macropore structure in bituminous and anthracite coal. *Fuel* **2018**, *223*, 32–43. [[CrossRef](#)]
22. Wang, Q.; Li, W.; Zhang, D.; Wang, H.; Jiang, W.; Zhu, L.; Tao, J.; Huo, P.; Zhang, J. Influence of high-pressure CO₂ exposure on adsorption kinetics of methane and CO₂ on coals. *J. Nat. Gas Sci. Eng.* **2016**, *34*, 811–822. [[CrossRef](#)]
23. Zhang, D.; Gu, L.; Li, S.; Lian, P.; Tao, J. Interactions of Supercritical CO₂ with Coal. *Energy Fuels* **2013**, *27*, 387–393. [[CrossRef](#)]
24. He, X.; Liu, X.; Nie, B.; Song, D. FTIR and Raman spectroscopy characterization of functional groups in various rank coals. *Fuel* **2017**, *206*, 555–563. [[CrossRef](#)]
25. Zhang, K.; Cheng, Y.; Li, W.; Wu, D.; Liu, Z. Influence of supercritical CO₂ on pore structure and functional groups of coal: Implications for CO₂ sequestration. *J. Nat. Gas. Sci. Eng.* **2017**, *40*, 288–298. [[CrossRef](#)]
26. Zhang, B.; Liang, W.; Ranjith, P.G.; Li, Z.; Li, C.; Hou, D. Coupling Effects of Supercritical CO₂ Sequestration in Deep Coal Seam. *Energy Fuels* **2018**, *33*, 460–473. [[CrossRef](#)]

27. Meng, M.; Qiu, Z. Experiment study of mechanical properties and microstructures of bituminous coals influenced by supercritical carbon dioxide. *Fuel* **2018**, *219*, 223–238. [[CrossRef](#)]
28. Day, S.; Fry, R.; Sakurovs, R. Swelling of Australian coals in supercritical CO₂. *Int. J. Coal Geol.* **2008**, *74*, 41–52. [[CrossRef](#)]
29. Zhang, X.G.; Ranjith, P.G.; Li, D.Y.; Perera, M.S.A.; Ranathunga, A.S.; Zhang, B.N. CO₂ enhanced flow characteristics of naturally-fractured bituminous coals with N₂ injection at different reservoir depths. *J. CO₂ Util.* **2018**, *28*, 393–402. [[CrossRef](#)]
30. Qu, H.; Liu, J.; Chen, Z.; Wang, J.; Pan, Z.; Connell, L.; Elsworth, D. Complex evolution of coal permeability during CO₂ injection under variable temperatures. *Int. J. Greenhouse Gas. Control.* **2012**, *9*, 281–293. [[CrossRef](#)]
31. Wang, K.; Du, F.; Wang, G. Investigation of gas pressure and temperature effects on the permeability and steady-state time of chinese anthracite coal: An experimental study. *J. Nat. Gas Sci. Eng.* **2017**, *40*, 179–188. [[CrossRef](#)]
32. Li, X.; Yan, X.; Kang, Y. Effect of temperature on the permeability of gas adsorbed coal under triaxial stress conditions. *J. Geophys. Eng.* **2018**, *15*, 386–396. [[CrossRef](#)]
33. Niu, S.; Zhao, Y.; Hu, Y. Experimental Investigation of the Temperature and Pore Pressure Effect on Permeability of Lignite Under the In Situ Condition. *Transp. Porous Med.* **2013**, *101*, 137–148. [[CrossRef](#)]
34. Yin, G.; Jiang, C.; Wang, J.G.; Xu, J. Combined Effect of Stress, Pore Pressure and Temperature on Methane Permeability in Anthracite Coal: An Experimental Study. *Transp. Porous Med.* **2013**, *100*, 1–16. [[CrossRef](#)]
35. Levy, J.H.; Day, S.J.; Killingley, J.S. Methane capacities of Bowen basin coals related to coal properties. *Fuel* **1997**, *76*, 813–819. [[CrossRef](#)]
36. Sakurovs, R.; Day, S.; Weir, S.; Duffy, G. Application of a modified Dubinin-Radushkevich equation to adsorption of gases by coals under supercritical conditions. *Energy Fuels* **2007**, *21*, 992–997. [[CrossRef](#)]
37. Crosdale, P.J.; Moore, T.A.; Mares, T.E. Influence of moisture content and temperature on methane adsorption isotherm analysis for coals from a low-rank, biogenically-sourced gas reservoir. *Int. J. Coal Geol.* **2008**, *76*, 166–174. [[CrossRef](#)]
38. Perera, M.S.A.; Ranjith, P.G.; Choi, S.K.; Airey, D. Investigation of temperature effect on permeability of naturally fractured black coal for carbon dioxide movement: An experimental and numerical study. *Fuel* **2012**, *94*, 596–605. [[CrossRef](#)]
39. Ozdemir, E. Modeling of coal bed methane (CBM) production and CO₂ sequestration in coal seams. *Int. J. Coal Geol.* **2009**, *77*, 145–152. [[CrossRef](#)]
40. Zhanli, R. Determination of heat flow in well Qincan 1 in Qinshui Basin, Shanxi province. *Chin. J. Geol.* **1998**, *2*, 251–254.
41. Angulo, R.F.; Alvarado, V.; Gonzalez, H. Fractal Dimensions from Mercury Intrusion Capillary Tests. In Proceedings of the SPE Latin America Petroleum Engineering Conference, Caracas, Venezuela, 8–11 March 1992; pp. 255–263.
42. Painter, P.C.; Snyder, R.W.; Starsinic, M.; Coleman, M.M.; Kuehn, D.W.; Davis, A. Concerning the Application of Ft-IR to the Study of Coal—A Critical-Assessment of Band Assignments and the Application of Spectral-Analysis Programs. *Appl. Spectrosc.* **1981**, *35*, 475–485. [[CrossRef](#)]
43. He, X.; Liu, X.; Song, D.; Nie, B. Effect of microstructure on electrical property of coal surface. *Appl. Surf. Sci.* **2019**, *483*, 713–720. [[CrossRef](#)]
44. Xuguang, S. The investigation of chemical structure of coal macerals via transmitted-light FT-IR microspectroscopy. *Spectrochim. Acta A Mol. Biomol. Spectrosc.* **2005**, *62*, 557–564. [[CrossRef](#)] [[PubMed](#)]
45. Hudot, B.B. *Coal and Gas Outburst*, 1st ed.; China Industrial Press: Beijing, China, 1966.
46. Cai, Y.; Liu, D.; Pan, Z.; Yao, Y.; Li, J.; Qiu, Y. Pore structure and its impact on CH₄ adsorption capacity and flow capability of bituminous and subbituminous coals from Northeast China. *Fuel* **2013**, *103*, 258–268. [[CrossRef](#)]
47. Zhao, W.; Cheng, Y.; Yuan, M.; An, F. Effect of Adsorption Contact Time on Coking Coal Particle Desorption Characteristics. *Energy Fuels* **2014**, *28*, 2287–2296. [[CrossRef](#)]
48. Ao, X.; Lu, Y.; Tang, J.; Chen, Y.; Li, H. Investigation on the physics structure and chemical properties of the shale treated by supercritical CO₂. *J. CO₂ Util.* **2017**, *20*, 274–281. [[CrossRef](#)]
49. Zhang, G.; Ranjith, P.G.; Perera, M.S.A.; Lu, Y.; Choi, X. Quantitative Analysis of Micro-structural Changes in a Bituminous Coal After Exposure to Supercritical CO₂ and Water. *Nat. Resour. Res.* **2019**, *28*, 1639–1660. [[CrossRef](#)]

50. Jiang, Y.; Luo, Y.; Lu, Y.; Qin, C.; Liu, H. Effects of supercritical CO₂ treatment time, pressure, and temperature on microstructure of shale. *Energy* **2016**, *97*, 173–181. [[CrossRef](#)]
51. Qin, C.; Jiang, Y.; Luo, Y.; Xian, X.; Liu, H.; Li, Y. Effect of Supercritical Carbon Dioxide Treatment Time, Pressure, and Temperature on Shale Water Wettability. *Energy Fuels* **2016**, *31*, 493–503. [[CrossRef](#)]
52. Zhang, K.; Cheng, Y.; Jin, K.; Guo, H.; Liu, Q.; Dong, J.; Li, W. Effects of Supercritical CO₂ Fluids on Pore Morphology of Coal: Implications for CO₂ Geological Sequestration. *Energy Fuels* **2017**, *31*, 4731–4741. [[CrossRef](#)]
53. Yin, H.; Zhou, J.; Jiang, Y.; Xian, X.; Liu, Q. Physical and structural changes in shale associated with supercritical CO₂ exposure. *Fuel* **2016**, *184*, 289–303. [[CrossRef](#)]
54. Friesen, W.I.; Mikula, R.J. Fractal Dimensions of Coal Particles. *J. Colloid Interface Sci.* **1987**, *120*, 263–271. [[CrossRef](#)]
55. Friesen, W.I.; Mikula, R.J. Mercury Porosimetry of Coals—Pore Volume Distribution and Compressibility. *Fuel* **1988**, *67*, 1516–1520. [[CrossRef](#)]
56. Gathitu, B.B.; Chen, W.Y.; McClure, M. Effects of Coal Interaction with Supercritical CO₂: Physical Structure. *Ind. Eng. Chem. Res.* **2009**, *48*, 5024–5034. [[CrossRef](#)]
57. Ouyang, Z.Q.; Liu, D.M.; Cai, Y.D.; Yao, Y.B. Fractal Analysis on Heterogeneity of Pore-Fractures in Middle-High Rank Coals with NMR. *Energy Fuels* **2016**, *30*, 5449–5458. [[CrossRef](#)]
58. Liu, X.; Song, D.; He, X.; Wang, Z.; Zeng, M.; Deng, K. Nanopore structure of deep-burial coals explored by AFM. *Fuel* **2019**, *246*, 9–17. [[CrossRef](#)]
59. Liu, S.; Sang, S.; Ma, J.; Wang, T.; Du, Y.; Fang, H. Effects of supercritical CO₂ on micropores in bituminous and anthracite coal. *Fuel* **2019**, *242*, 96–108. [[CrossRef](#)]
60. Wang, Q.; Ye, J.-B.; Yang, H.-Y.; Liu, Q. Chemical Composition and Structural Characteristics of Oil Shales and Their Kerogens Using Fourier Transform Infrared (FTIR) Spectroscopy and Solid-State ¹³C Nuclear Magnetic Resonance (NMR). *Energy Fuels* **2016**, *30*, 6271–6280. [[CrossRef](#)]
61. Ibarra, J.V.; Moliner, R.; Bonet, A.J. Ft-Ir Investigation on Char Formation during the Early Stages of Coal Pyrolysis. *Fuel* **1994**, *73*, 918–924. [[CrossRef](#)]
62. Nie, B.; Liu, X.; Yang, L.; Meng, J.; Li, X. Pore structure characterization of different rank coals using gas adsorption and scanning electron microscopy. *Fuel* **2015**, *158*, 908–917. [[CrossRef](#)]
63. Ouyang, Z.; Liu, D.; Cai, Y.; Yao, Y. Investigating the Fractal Characteristics of Pore-Fractures in Bituminous Coals and Anthracites through Fluid Flow Behavior. *Energy Fuels* **2016**, *30*, 10348–10357. [[CrossRef](#)]
64. Fu, Y.; Liu, X.; Ge, B.; Liu, Z. Role of chemical structures in coalbed methane adsorption for anthracites and bituminous coals. *Adsorption* **2017**, *23*, 711–721. [[CrossRef](#)]
65. Castro-Marcano, F.; Lobodin, V.V.; Rodgers, R.P.; McKenna, A.M.; Marshall, A.G.; Mathews, J.P. A molecular model for Illinois No. 6 Argonne Premium coal: Moving toward capturing the continuum structure. *Fuel* **2012**, *95*, 35–49. [[CrossRef](#)]
66. Chamberlain, E.A.C.; Barrass, G.; Thirlaway, J.T. Gases Evolved and Possible Reactions during Low-Temperature Oxidation of Coal. *Fuel* **1976**, *55*, 217–223. [[CrossRef](#)]
67. Mazumder, S.; Vanhemert, P.; Bruining, J.; Wolf, K.; Drabe, K. In situ CO₂–coal reactions in view of carbon dioxide storage in deep unminable coal seams. *Fuel* **2006**, *85*, 1904–1912. [[CrossRef](#)]
68. Kolak, J.J.; Hackley, P.C.; Ruppert, L.F.; Warwick, P.D.; Burruss, R.C. Using Ground and Intact Coal Samples To Evaluate Hydrocarbon Fate during Supercritical CO₂ Injection into Coal Beds: Effects of Particle Size and Coal Moisture. *Energy Fuels* **2015**, *29*, 5187–5203. [[CrossRef](#)]

